PAPER

Check for updates

Star-PCL shape memory polymer (SMP) scaffolds with tunable transition temperatures for enhanced utility†

Courteney T. Roberts, [ID] [a] Sarah K. Beck, [ID] [a] C. Mabel Prejean, [a] Lance M. Graul, [a] Duncan J. Maitland [ID] [a] and Melissa A. Grunlan [ID] *[abc]

Thermoresponsive shape memory polymers (SMPs) prepared from UV-curable poly(ε-caprolactone) (PCL) macromers have the potential to create self-fitting bone scaffolds, self-expanding vaginal stents, and other shape-shifting devices. To ensure tissue safety during deployment, the shape actuation temperature (*i.e.*, the melt transition temperature or T_m of PCL) must be reduced from ~ 55 °C that is observed for scaffolds prepared from *linear*-PCL-DA ($M_n \sim 10$ kg mol^{-1}). Moreover, increasing the rate of biodegradation would be advantageous, facilitating bone tissue healing and potentially eliminating the need for stent retrieval. Herein, a series of six UV-curable PCL macromers were prepared with *linear* or 4-arm *star* architectures and with M_ns of 10, 7.5, and 5 kg mol^{-1}, and subsequently fabricated into six porous scaffold compositions (10kℓ, 7.5kℓ, 5kℓ, 10k★, 7.5k★, and 5k★) *via* solvent casting particulate leaching (SCPL). Scaffolds produced from *star*-PCL-tetraacrylate (*star*-PCL-TA) macromers produced pronounced reductions in T_m with decreased M_n *versus* those formed with the corresponding *linear*-PCL-diacrylate (*linear*-PCL-DA) macromers. Scaffolds were produced with the desired reduced T_m profiles: 37 °C < T_m < 55 °C (self-fitting bone scaffold), and $T_m \leq$ 37 °C (self-expanding stent). As macromer M_n decreased, crosslink density increased while % crystallinity decreased, particularly for scaffolds prepared from *star*-PCL-TA macromers. While shape memory behavior was retained and radial expansion pressure increased, this imparted a reduction in modulus but with an increase in the rate of degradation.
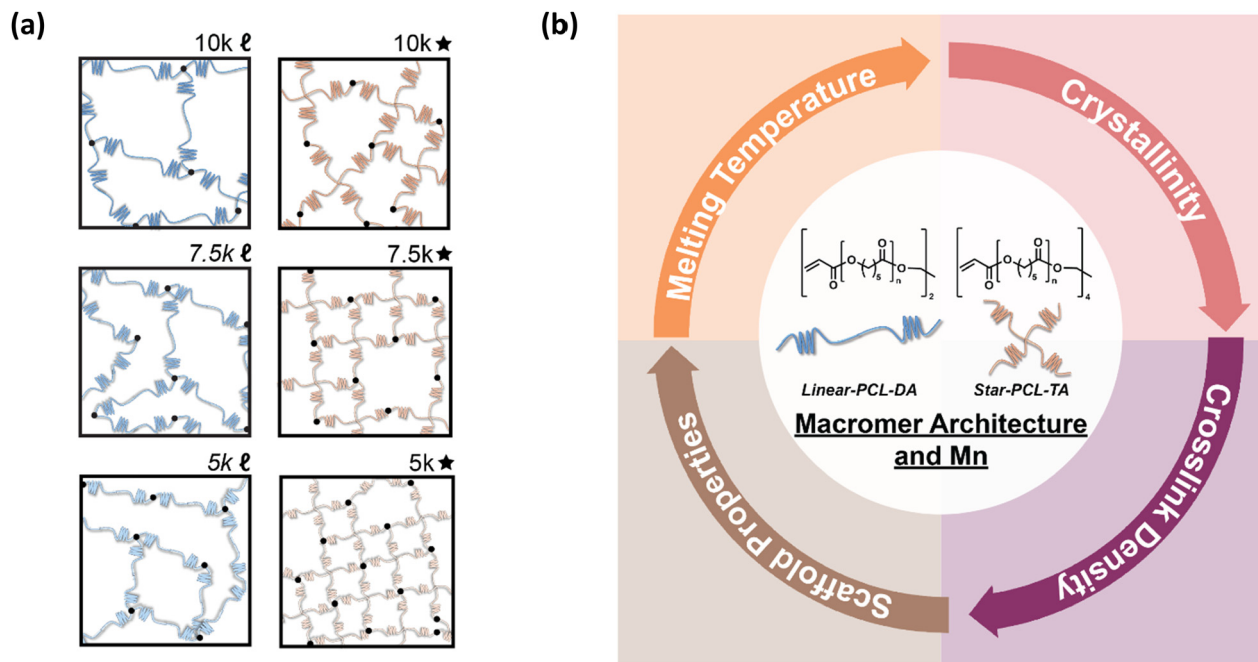
Introduction

Thermoresponsive shape memory polymers (SMPs) have been widely explored for biomedical applications.[1,2] Biodegradable, semi-crystalline poly(ε-caprolactone) (PCL) SMPs[3,4] have been proposed for numerous biomedical applications including 'self-closing sutures', and 'self-expanding' cardiovascular stents.[5,6] We developed 'self-fitting' PCL-based scaffolds for bone regeneration.[7] UV-curable PCL macromers afford convenient fabrication of such devices. For instance, we utilized *linear*-PCL-diacrylate (*linear*-PCL-

a Department of Biomedical Engineering, Texas A&M University, College Station, Texas 77843, USA. E-mail: mgrunlan@tamu.edu

b Department of Materials Science and Engineering, Texas A&M University, College Station, Texas 77843, USA

c Department of Chemistry, Texas A&M University, College Station, Texas 77843, USA

† Electronic supplementary information (ESI) available: NMR spectra, DSC data, crosslink density tests, macromer solution viscosity and diffusion through salt template, sol content, porosity, thermal properties, shape fixity & recovery, radial expansion pressures, degradation data, and mechanical data. See DOI: https://doi.org/10.1039/d4tb00050a

DA, $M_n \sim 10$ kg mol^{-1}) to prepare porous scaffolds *via* the UV cure of a solvent-based solution over a fused salt template followed by aqueous extraction of the template (*i.e.*, solvent-casting/particulate leaching, SCPL).[7,8] In the resulting PCL networks, the covalent crosslinks act as net points while the crystalline lamellae act as switching segments. These scaffolds exhibited a melt transition (T_m) of ~ 55 °C, such that when heated ($T > T_m$), the crystalline lamellae melt causing the scaffold to become soft and malleable. This allows the scaffold to press-fit into irregular defects, with shape recovery driving expansion to the perimeter. Shape fixity occurs when the scaffold is subsequently cooled to body temperature (~ 37 °C) ($T < T_m$). These conformal, self-fitting PCL SMP scaffolds have demonstrated excellent osseointegration and healing in a preclinical study,[9] and so represent a potential alternative to existing biological and alloplastic grafts.

The T_m of PCL SMPs is vital as it serves as the actuation temperature for shape recovery during implantation. Due to the risk of thermal damage to tissues,[10–13] systematically reducing the T_m of PCL SMP scaffolds is necessary. In the case of bone scaffolds prepared from *linear*-PCL-DA ($M_n \sim 10$ kg mol^{-1}), a T_m of 55 °C prohibits surgical site irrigation to extend the

Fig. 1 To achieve porous PCL SMP scaffolds with systematically lower, "tissue safe" shape transition temperatures (T_m), (a) *linear*-PCL-DA and *star*-PCL-TA UV-curable macromers of varying M_ns (10, 7.5, and 5 kg mol^{-1}) were synthesized and used to prepare a series of 6 scaffolds: 10kℓ, 7.5kℓ, 5kℓ, 10k★, 7.5k★, and 5k★. (b) Alternations to macromer architecture and M_n produced changes in T_m, % crystallinity, and crosslink density that in turn produced changes in scaffold properties (*e.g.*, mechanical and degradation).

working time. Ideally, such a scaffold would exhibit a 37 °C < T_m < 55 °C so that, once fitted, would return to the rigid state to support load. We also recently proposed porous, self-expanding vaginal stents that could be inserted in a fixed, compressed state, and then shape recovered *in situ* to provide patency.[14,15] Such a device would require a T_m ≤ 37 °C. Other devices would also ideally shape recovery at body temperature (*e.g.*, vascular stents, surgical sutures, *etc.*). Overall, systematic reductions in the T_m values of PCL SMPs would represent a significant enhancement in tissue safety and hence utility.

The % crystallinity and T_m values of polymers is known to be influenced by architecture as well as molecular weight (M_n).[16,17] *Versus* analogous *linear* polymers of the same M_n, the lower steric mobility and shorter chain length of multi-arm polymers reduce crystallization.[18–20] This effect has been observed for specifically *star* homopolymers (*i.e.*, 4-arm extending from a central core).[19–24] We have reported that *star*-PCL-tetracrylate (*star*-PCL-TA, M_n ~ 10 kg mol^{-1}) exhibited a significantly lower T_m (~45 °C) *versus* its *linear* analogue (*linear*-PCL-DA, M_n ~ 10 kg mol^{-1}; ~55 °C).[25] Because of the concomitant deduction in % crystallinity, *star*- polyesters have been utilized to tailor rates of degradation.[26–28] Indeed, a faster rate of degradation was noted for scaffolds prepared from *star*-PCL-TA (M_n ~ 10 kg mol^{-1}) *versus linear*-PCL-DA (M_n ~ 10 kg mol^{-1}). Lastly, *star*- polymers are well known for having relatively reduced dilute solution viscosities, due to their reduced hydrodynamic volumes and fewer chain entanglements,[19,20,29,30] which can be helpful in solvent-based fabrication processes.

Herein, towards tuning the T_m of PCL-based SMP scaffolds to afford greater utility and tissue safety, the architecture and M_n of UV curable macromers were systematically tuned (Fig. 1). PCL macromers were prepared with *linear*- and *star*- architectures, and M_n was modulated in increments of 2500 g mol^{-1}. From this, the following six scaffold compositions were prepared from the designated macromer: 10kℓ (*linear*-PCL-DA, M_n ~ 10 kg mol^{-1}), 7.5kℓ (*linear*-PCL-DA, M_n ~ 7.5 kg mol^{-1}), 5kℓ (*linear*-PCL-DA, M_n ~ 5 kg mol^{-1}), 10k★ (*star*-PCL-TA, M_n ~ 10 kg mol^{-1}), 7.5k★ (*star*-PCL-TA, M_n ~ 7.5 kg mol^{-1}), and 5k★ (*star*-PCL-TA, M_n ~ 5 kg mol^{-1}). All porous scaffolds were prepared *via* SCPL to generate similar pore sizes as well as pore interconnectivity. These six SMP scaffold compositions were then assessed in terms of rheological, thermal, shape memory, degradative, and mechanical properties towards advancing their use as tissue-safe self-fitting bone scaffolds, self-expanding vaginal stents, as well as potentially other SMP devices.

Experimental

Materials

Linear-PCL-diol (M_n = 10 kg mol^{-1} per manufacturer), ε-caprolactone, pentaerythritol, tin(II) 2-ethylhexanoate (Sn(Oct)$_2$), ethylene glycol, dichloromethane (DCM), 4-(dimethylamino)pyridine (DMAP), triethylamine (Et$_3$N), acryloyl chloride, ethyl acetate, potassium carbonate (K$_2$CO$_3$), anhydrous magnesium sulfate (MgSO$_4$), sodium chloride (NaCl) salt, 2,2-dimethoxy-2-phenyl acetophenone (DMP), 1-vinyl-2-pyrrolidinone (NVP), sodium hydroxide (NaOH), deuterated chloroform (CDCl$_3$), phosphate-buffered saline (PBS), and solvents were obtained from Sigma-Aldrich. All solvents were dried over 4 Å molecular sieves, all

This journal is © The Royal Society of Chemistry 2024

J. Mater. Chem. B, 2024, **12**, 3694–3702 | **3695**

reagents were vacuum dried overnight (ON), and all glassware and stir bars were dried at 120 °C ON prior to use. Salt was sieved to an average size of 460 ± 70 μm (per scanning electron microscopy [SEM] and ImageJ) using an ASTM E-11 no. 40 and no. 35 sieves with 425 μm and 500 μm openings, respectively.

Methods

Syntheses. All reactions were run under a nitrogen (N_2) atmosphere with a Teflon-covered stir bar. After purification, molecular structures (including % acrylation, architecture, and M_n) were determined with ^{1}H NMR spectroscopy (Avance Neo 400 MHz spectrometer) operating in the FT-mode with CDCl$_3$ as the standard (Fig. S1 and S2, ESI†). The target M_n and architecture of *linear*-PCL-DA and *star*-PCL-TA macromers were verified by comparing the repeat unit CH_2 δ = 4.1 ppm *versus* the terminal CH_2 δ = 3.7 ppm. Differential scanning calorimetry (DSC, TA Instruments Q100) protocols described below were used to determine thermal properties.

Linear-PCL-diol (10 kg mol^{-1}) was purchased while *linear*-PCL-diols (7.5 and 5 kg mol^{-1}) were synthesized *via* ring-opening polymerization (ROP) as follows. ε-Caprolactone (20.0 g), a difunctional initiator (ethylene glycol), and Sn(Oct)$_2$ were combined in a round bottom (rb) flask and maintained at 120 °C ON. The targeted M_ns were achieved by adjusting the monomer to initiator molar ratio: 88 : 1 [10 kg mol^{-1}], 66 : 1 [7.5 kg mol^{-1}], and 44 : 1 [5 kg mol^{-1}]. The crude product was dissolved in DCM, precipitated into methanol, vacuum filtered, and dried (room temperature [RT], overnight [ON], 30 in. Hg) to obtain the purified product. *Star*-PCL-tetrols (10, 7.5, and 5 kg mol^{-1}) were likewise prepared *via* the Sn(Oct)$_2$-catalyzed ROP of ε-caprolactone (20.0 g), but in the presence of a tetrafunctional initiator (pentaerythritol), and at the designated monomer to initiator molar ratios: 88 : 1 [10 kg mol^{-1}], 66 : 1 [7.5 kg mol^{-1}], and 44 : 1 [5 kg mol^{-1}]. The final products were likewise isolated.

Linear-PCL-diols and *star*-PCL-tetrols were acrylated to form UV-curable *linear*-PCL-DA and *star*-PCL-TA macromers, respectively, using established acrylation protocols.[8] Briefly, each diol (20.0 g) was combined with DMAP (6.6 mg for *linear*-PCL-diols; 13.2 mg for *star*-PCL-tetrols) and dissolved in DCM (120 mL). Et$_3$N and acryloyl chloride (4.0 mmol & 8.0 mmol for *linear*-PCL-diols; 8.0 mmol & 16.0 mmol for *star*-PCL-tetrols) were each added dropwise to the flask and stirred under positive N_2 pressure for 30 min at RT. Established work-up procedures[8] were followed to obtain *linear*-PCL-DA and *star*-PCL-TA. The final products were isolated as above.

Fabrication

Scaffolds. Porous scaffolds (10kℓ, 7.5kℓ, 5kℓ, 10k★, 7.5k★, and 5k★) were fabricated using a SCPL protocol per previous reports.[7,8,25] Briefly, sieved NaCl (10 g; 460 ± 70 μm) was placed into a 20 mL scintillation vial (I.D. = 25 mm). DI water (7.5 wt%) was added in four parts followed by manual stirring after each addition. The wet salt was then compacted using a glass stir rod and the vials centrifuged (15 min, 3220 rpm). The open vials were then air-dried (~1 h) and vacuum dried (RT, ON, 30 in. Hg).

Macromer solutions were prepared by dissolving the designated acrylated macromer in DCM (0.15 g total per mL DCM). Next, photoinitiator solution (10 wt% DMP in NVP) was added at 15 vol%. To each salt template, 5 mL of the resulting solution were added to a vial containing the fused salt template and subsequently centrifuged (10 min, 1260 rpm). Crosslinking of the acrylated macromers was afforded by exposing open vials to UV light for 6 min (UV-Transilluminator, 6 mW cm^2, 365 nm). Opened vials were then left in the fume hood to air dry ON. Next, to remove the salt template, vials were placed in a 1 : 1 ratio of water to ethanol for ~5 days with daily solution changes. Scaffolds were dried in the fume hood ON, and then heat-treated (85 °C, 1 h, 30 in. Hg). The resulting cylindrical scaffolds ($d \sim$ 12 mm) were sequentially sliced into three specimens ($t \sim$ 2 mm) (Vibratome, Leica VT 1000 S) and biopsy punched (Integra Miltex, $d \sim$ 6 mm). The final dimension of a scaffold disc specimen was $d \sim$ 6 mm × $t \sim$ 2 mm.

Films. Analogous solid films (10kℓ, 7.5kℓ, 5kℓ, 10k★, 7.5k★, and 5k★) were prepared for crosslink density and % porosity calculations. Macromer solutions were prepared (0.43 g total per mL DCM), and a designated solution added to a circular silicone mold ($d \sim$ 45 mm × $t \sim$ 2 mm; McMaster-Carr) secured between two glass slides. The mold was then exposed to UV-light (UV Transilluminator, 6 mW cm^2, 365 nm) for 3 min on each side. The swollen films were sequentially air-dried (RT, ON), dried *in vacuo* (RT, 4 h, 30 in. Hg), soaked in ethanol atop a shaker table (150 rpm, 4 h), air dried (RT, ON), and heat-treated *in vacuo* (85 °C, 1 h, 30 in. Hg). Films were biopsy punched to form final disc specimens ($d \sim$ 4 mm × $t \sim$ 1.5 mm).

Crosslink density

Crosslink density was analyzed *via* a swelling test on solid film discs (N = 3). Each disc was submerged in 10 mL of DCM for 24 h in a sealed vial. Solvent-swollen discs were removed, diameters immediately determined with an electronic caliper, and specimens photographed. Solvent-swollen discs were subsequently dried *in vacuo* (RT, ON, 30 in. Hg.), diameters likewise recorded, and photographed.

Macromer solution viscosity and diffusion through salt template

The reduced viscosities (η_{red}) of macromer (*i.e.*, *linear*-PCL-DA and *star*-PCL-TA) solutions were determined using a Cannon-Fenske viscometer (size 200). Macromer solutions were created at incremental concentrations (0.075, 0.150, 0.225, and 0.300 g mL^{-1} in DCM), and tested in triplicate per concentration (N = 3). Solutions (10 mL) were poured into the viscometer and maintained at 25 °C using a surrounding water bath. A stopwatch was used to measure the efflux time of each solution through the designated region. The η_{red} of each solution may be expressed and calculated per the following equation:

$$\eta_{red} = \frac{t - t_0}{t_0 \times c} = \frac{\eta_{sp}}{c} \qquad (1)$$

where η_{sp} is the specific viscosity, c is the concentration of the macromer solution, t is the efflux time, and t_0 is the efflux time of the solvent.

Dye-containing macromer solutions were used to analyze the relative differences in diffusion rates through a salt template during a SCPL fabrication process. For improved visual observation, taller salt molds were prepared as above but with increased amount of sieved NaCl (~ 15 g). A macromer solution (~ 7.5 mL) containing the photoinitiator was prepared as above, to which a few drops of blue food coloring was added. Two salt templates were placed side-by-side while the *linear-* and *star-* macromer solutions of the same M_n were simultaneously poured over the template, and diffusion recorded by video.

Sol content

Scaffold disc specimens ($N = 3$) were each submerged into 10 mL of DCM in a scintillation vial. Vials were sealed and placed atop a shaker plate (48 h, 150 rpm). Next, scaffolds were removed, rinsed with DCM, air dried (~ 2 h), and dried *in vacuo* (RT, ON, 30 in. Hg). Initial and final masses were used to calculate the % sol (*i.e.*, % mass loss).

Morphology

Pore size and interconnectivity. SEM (Tescan Vega 3, Au–Pt sputter coating (~ 14 nm), accelerating voltage ~ 10 kV) was used to analyze pore size and pore interconnectivity. Scaffold images ($N = 3$) were analyzed using ImageJ, with measurements ($N = 12$) taken from pores along the diagonal midline to determine the average pore size.

% Porosity. Scaffold % porosity was gravimetrically determined ($N = 3$) from the densities of solid films ($\rho_{solid\ film}$) and corresponding porous scaffolds ($\rho_{porous\ scaffold}$) per eqn (2):

$$\text{Porosity}(\%) = \frac{\rho_{solid\ film} - \rho_{porous\ scaffold}}{\rho_{solid\ film}} \times 100 \qquad (2)$$

% Pore interconnectivity. Scaffold specimens ($N = 3$) were evaluated to determine their pore interconnectivity using a water wicking protocol.[31] Specimens were individually submerged in 10 mL DI water in a sealed vial, and placed on a shaker plate (24 h, 150 rpm) to expel any air bubbles within pores. Specimens were then removed, and weighed on a Petri dish (Mass$_{total}$). To wick away the water within the interconnected pore volume, a folded Kimwipe was gently pressed onto the surface of the specimen for 1 min, and the specimen was weighed (Mass$_{interconnected}$). The % pore interconnectivity was calculated *via* eqn (3):

$$\text{Interconnectivity}(\%) = \frac{\text{Mass}_{total} - \text{Mass}_{interconnected}}{\text{Mass}_{total}} \times 100 \quad (3)$$

T_m and % crystallinity

DSC (TA Instruments Q100) was used to characterize T_m and % crystallinity of diols and tetrols, acrylated macromers, and scaffolds. Each specimen (~ 10 mg; $N = 3$) was sealed in a hermetic pan, and heated/cooled (5 °C min^{-1}) over two cycles. The endothermic melt peak was characterized in terms of the onset ($T_{m,onset}$) and midpoint (T_m) values (TA Universal Analysis Software). Reported values were determined using the second cycle to account for removal of thermal history. Eqn (4) was used to quantify PCL % crystallinity:

$$\%X_c = \frac{\Delta H_m - \Delta H_c}{\Delta H_c^\circ} \qquad (4)$$

where ΔH_m is the enthalpy of fusion calculated from the integral of the endothermic melt peak, ΔH_c is the enthalpy of crystallization from the exothermic cold crystallization peak, and ΔH_c° is the theoretical value for 100% crystalline PCL (139.5 J g^{-1}).[32]

Shape memory properties

Shape fixity and recovery. Shape memory properties of scaffold specimens ($N = 3$) were evaluated using a model defect as previously described.[25] A circular defect ($d \sim 5$ mm) was created from an UHMWPE sheet ($t \sim 2$ mm) using a drill press (Grizzly G7948). A hot plate equipped with a digital temperature probe (Heidolph, MR HEI-TEC) was used to pre-heat saline to the designated T_m. Each scaffold specimen was subjected to the following protocol, and the diameter recorded as noted with an electronic calipers to quantify scaffold strain (ε): (1) record diameter; (2) submerge into the water bath at the designated T_m (~ 1 min); (3) remove from the water bath and immediately press fit into the model defect (at RT); (4) maintain in the defect for ~ 2 min to allow for shape fixity; (5) remove from the defect, and allowed to sit for ~ 2 min (at RT); (6) record diameter; (7) re-submerge into the water bath at designated T_m (~ 1 min) to allow for shape recovery; (8) remove from the water bath and cool for ~ 2 min (at RT); (9) record diameter. This procedure was repeated twice to determine shape fixity (R_f) and shape recovery (R_r) over for the first ($N = 1$) and second ($N = 2$) cycles according to their respective equations.

$$R_f(N) = \frac{\varepsilon_u(N)}{\varepsilon_m} \times 100 \qquad (5)$$

$$R_r(N) = \frac{\varepsilon_i(N)}{\varepsilon_r(N)} \times 100 \qquad (6)$$

where $\varepsilon_u(N)$ is the strain in the stress-free state, ε_m is the maximum strain, $\varepsilon_i(N)$ is the initial strain is a stress-free environment, and $\varepsilon_r(N)$ is the recovered strain in a stress-free environment.

Radial pressure during shape recovery. Scaffold discs ($N = 5$) were subjected to radial mechanical testing (Instron 5965 equipped with a clockwise RJA62 J-crimp Radial Compression Station) per a prior reported.[25] This protocol was utilized to determine the radial pressure exerted by a scaffold during shape recovery at its designated T_m to mimic press-fitting into a defect ($d \sim 4.5$ mm). Each specimen was loaded into the bore ($d \sim 6.5$ mm), heated to the T_m, and maintained for 5 min. The bore then compressed to $d \sim 4.5$ mm at a rate of 1 mm min^{-1}. At this point, force was recorded, total radial force (TRF) calculated, and TRF converted to radial pressure based on scaffold dimensions.[33]

This journal is © The Royal Society of Chemistry 2024

J. Mater. Chem. B, 2024, **12**, 3694–3702 | **3697**

Degradation

Degradation studies under accelerated conditions were performed according to ASTM F1635. Scaffold specimens (N = 3 per time point) were each submerged in 10 mL of 0.1 M NaOH in a 20 mL glass scintillation vials. The sealed vials were placed in an incubator (VWR Benchtop Shaking Incubator, Model 1570), and maintained at 37 °C and 60 rpm. At the designated time points (1, 2, 3, 4, 5, 6, 7, 8, 9, 10, 12, and 15 days), specimens were removed, rinsed well with DI water, and dried *in vacuo* (RT; ON; 36 in. Hg). The final dried mass was compared to the initial mass to determine the mass loss. SEM images of specimens at 7 days were obtained as described above.

Compressive mechanical properties

Scaffold specimens (N = 5) underwent static compression testing (Instron 5944) at RT with a constant rate of strain (1.5 mm min^{-1}) up to 85% strain (ε). Due to their non-brittle nature, no specimen fractured. The compressive modulus (E), strength (CS), and toughness were determined. From the resulting stress (σ) *versus* ε curve, and E was calculated from the initial *linear* region ($\leq$10% ε). CS was determined at 85% ε. Toughness values were calculated from the areas under the σ *vs.* ε curves.

Statistical analysis

All data was reported as the average ± the standard deviation. Statistical analysis was performed using one-way analysis of variance (ANOVA) between compositions of similar architecture followed by Welches *t*-test to make direct comparisons between ℓ *vs.* ★ compositions at the same M_n. 10kℓ and 10k★ were used as the respective controls during the ANOVA tests. A *p*-value of * < 0.05 was considered statistically significant.

Results and discussion

Macromer synthesis

Linear-PCL-diols, *star*-PCL-tetrols, *linear*-PCL-DAs, and *star*-PCL-TAs were characterized *via* ^{1}H NMR to confirm molecular structure and M_ns as well as by DSC to evaluate thermal properties (Fig. S1 and S2, ESI†). The targeted M_ns (10, 7.5, and 5 kg mol^{-1}) were achieved by modulating the ratio of monomer to di- or tetrafunctional initiator. For a given M_n, end group analysis verified *linear versus star* architecture due to the doubling of end group protons for the latter. Spectra also confirmed that diols and tetrols were successfully acrylated (>85%). For *linear*-PCL-diols and *linear*-PCL-DAs, T_m [~53–54 °C] and % crystallinity [~46–53%] were not substantially impacted by M_n. This was also the case for the T_m [~44–49 °C] and % crystallinity [~42–50%] values of *star*-PCL-diols and *star*-PCL-TAs.

Crosslink density

Prior to fabrication of porous scaffolds, solid films were produced by acrylated macromers to determine relative crosslink density. Diminished swelling (*i.e.*, decreased % diameter change) was expected as crosslink density increased. As macromer M_n decreased, crosslink density would increase. Also, for a given M_n, crosslink density would increase for *star- versus linear-* macromers. These expected trends were observed (Fig. S3 and Table S1, ESI†). Notably, for a given M_n, the films based on *star-* macromers exhibited significantly less swelling. In this way, differences in crosslink density produced by macromers can be used to subsequently explain properties of crosslinked scaffolds.

Solution viscosity and diffusion

Polymers with a *star* architecture are known to have a lower hydrodynamic volume and hence lower solution viscosity *versus* a *linear* analogue of the same M_n.[19,20,29,30] Thus, the η_{red} values of acrylated macromer solutions were determined to further verify architecture (Fig. S4 and Table S2, ESI†). This expected trends were generally observed, with *star*-PCL-TAs (10 and 7.5 kg mol^{-1}) having lower η_{red} *versus* the corresponding *linear*-PCL-DAs. The reduced viscosities of *star*-PCL-TA (5 kg mol^{-1}) and *linear*-PCL-TA (5 kg mol^{-1}) were quite similar, perhaps due to their low M_n and hence short arm lengths. As expected, η_{red} values decreased as macromer M_n decreased.

A lower η_{red} was expected to facilitate scaffold fabrication by enhancing the rate of diffusion of the macromer solution through the fused salt template during SCPL. To observe this, macromer solutions containing a dye were cast over templates to assess relative diffusion rates (Fig. S5, ESI†). As anticipated, macromer solutions based on *star*-PCL-TAs exhibited faster diffusion *versus* those based on *linear*-PCL-TAs of the same M_n with rates increasing as M_n decreased. While the scaffold fabrication protocol used herein utilized centrifugation to ensure that macromer solutions diffused completed through a salt template, the η_{red} exhibited by *star* macromers could be advantageous for preparing larger scaffolds that cannot be subjected to centrifugation.

Scaffold fabrication and porosity

Scaffolds were fabricated *via* SCPL from *linear*-PCL-DA and *star*-PCL-TA macromers to produce six compositions based on architecture and M_n: 10kℓ, 7.5kℓ, 5kℓ, 10k★, 7.5k★, and 5k★. Sol content studies confirmed successful crosslinking of macromers, with all compositions displaying low sol content (< ~5%) (Fig. S6 and Table S3, ESI†). Analysis of SEM images (Fig. S7a, ESI†) revealed that scaffold average pore sizes (~190 μm) were largely similar (Fig. S7b and Table S4, ESI†). This pore size range is within that associated with osseointegration and subsequent vascularization between the host bone and scaffold,[34] but could be modulated *via* salt size if preferred for other applications. Scaffolds exhibited ~64–77% porosity (Fig. S7c and Table S4, ESI†). The use of the fused salt template during SCPL fabrication resulted in scaffolds with similar average pore interconnectivity (~51%) (Fig. S8 and Table S4, ESI†). In the case of bone regeneration, this feature is anticipated to enhance cellular infiltration and neotissue formation throughout the scaffold. For vaginal stents, pore interconnectivity should facilitate egress.

3698 | *J. Mater. Chem. B*, 2024, **12**, 3694–3702

This journal is © The Royal Society of Chemistry 2024

Scaffold T_m and % crystallinity

T_m is a vital aspect of shape memory PCL scaffolds as it represents the temperature required for self-fitting (*e.g.*, within bone defects) and self-expansion (*e.g.*, as a stent within the vaginal canal). As noted earlier, a self-fitting scaffold to treat bone detects would ideally exhibit $37\ ^\circ C < T_m < 55\ ^\circ C$, thus permitting continued irrigation at the defect site without necrosis (to prolong the fitting time), but subsequently returning to a rigid state to support load. In the case of a self-expanding vaginal stent, a $T_m < 37\ ^\circ C$ would permit insertion in a fixed, compressed state followed by expansion. A reduction in PCL % crystallinity is expected to give rise to lower T_m values. The T_m and % crystallinity of scaffolds were obtained from DSC thermograms (Fig. 2 and Table S5, ESI†). A reduction in M_n of *linear*-PCL-DA did not lead to a significant decrease in scaffold T_m ($\sim$51–56 °C) despite the decrease in % crystallinity: 10kℓ ($\sim$46%) *versus* 7.5kℓ ($\sim$37%) and 5kℓ ($\sim$35%). Thus, no *linear*-scaffold exhibited the desirable thermal profile. In contrast, scaffolds prepared from *star*-PCL-TAs of decreasing M_n exhibited a pronounced and systematic decrease in T_m and % crystallinity: 10k★ ($\sim$46 °C/$\sim$27%), 7.5k★ ($\sim$40 °C/$\sim$22%), and 5k★ ($\sim$29 °C/$\sim$19%). Furthermore, for a given M_n, these values were lower for *star*- scaffolds *versus* *linear*- scaffolds. This reduction is attributed to the shorter length of *star* "arms" (*i.e.*, higher crosslink density) that limits the potential to form crystalline lamellae, a phenomena observed in other semi-crystalline polymers.[19–24] Based on achieved T_m values, specific compositions emerged as candidates for the aforementioned tissue-safe applications: 10k★ and 7.5k★ (self-expanding bone tissue scaffold), and 5k★ (self-expanding stent). Still, the differences in scaffold % crystallinity and crosslink density was expected to impact other key properties as detailed below.

Shape memory behavior and radial expansion pressure

Given the role of crystalline lamellae as switching segments in shape memory behavior, it is paramount that scaffolds retain sufficient % crystallinity. Shape memory tests were performed using a circular model defect ($d \sim$ 5 mm). Slightly oversized scaffold specimens ($d \sim$ 6 mm) were used to ensure contact with the defect perimeter. The model defect diameter also coincides with the dimensions of a rat calvarial defect model often used in preliminary assessment of bone regeneration.[35,36] Thus, the protocol mimics how scaffolds would undergo self-fitting in such defects, with the scaffold's T_m (midpoint) used as the temperature of the saline bath. As detailed in the methods, shape fixity (R_f) was related to retention of new diameter following fitting into and removal from defect while shape recovery (R_r) was related to subsequent recovery of original diameter. R_f and R_r were measured over 2 cycles. While the % crystallinity of *linear*- scaffolds ($\sim$35–47%) was greater than that of *star*-scaffolds ($\sim$19–27%), shape memory behavior was retained with R_f and R_r values near $\sim$100% for all compositions (Table S6, ESI†). Based on visual observations, the 5k★ had slightly diminished R_f values, attributed to its low % crystallinity.

The radial pressure exerted by such a scaffold specimen ($d \sim$ 6 mm) during shape recovery was evaluated upon placing
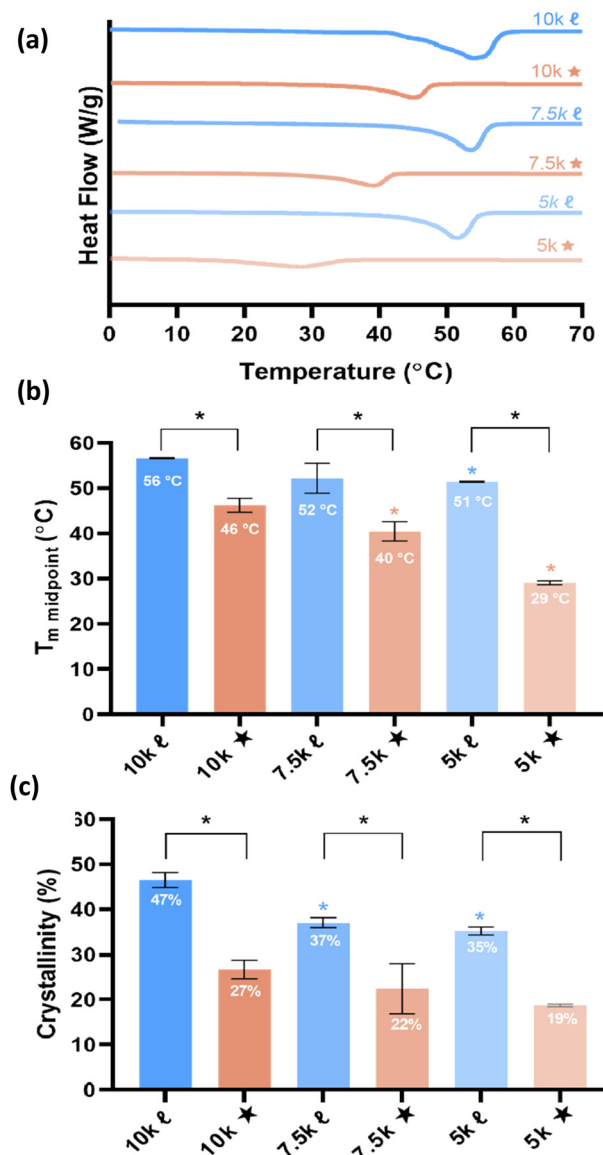

Fig. 2 (a) Representative DSC thermograph of scaffolds. (b) T_m values. (c) % Crystallinity values. "Black *" $p < 0.05$ comparing *linear*- and *star*- scaffolds of same M_n. "Blue *" $p < 0.05$ *versus* 10kℓ. "Pink *" $p < 0.05$ *versus* 10k★.

into a bore, equilibrating at its T_m (midpoint), and reducing the diameter ($d \sim$ 4.5 mm) (Fig. 3a). It was expected that as crosslink density increased (*i.e.*, macromer M_n decreased), radial pressure would increase.[37] However, *linear*- scaffolds exhibited statistically similar radial pressures ($\sim$100 kPa) (Fig. 3b and Table S7, ESI†). At a given M_n, *star*- scaffolds did exhibit greater radial pressures ($\sim$156–273 kPa) *versus linear*- scaffolds, which may be attributed to more rapid melting of lamellae. Radial pressures of 7.5k★ and 5k★ were lower *versus* that of 10k★ due to the reduction in % crystallinity.

Degradation behavior

The slow degradation of PCL *in vivo* ($\sim$2 years)[38] is generally limiting to resorbable device development, such that faster as well as tunable rates of degradation would enhance its utility.
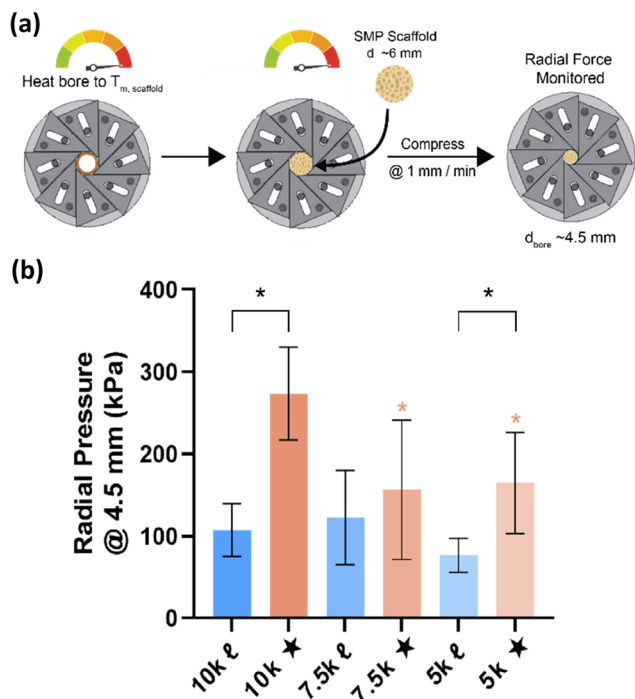
This journal is © The Royal Society of Chemistry 2024

J. Mater. Chem. B, 2024, **12**, 3694–3702 | **3699**

Fig. 3 (a) Protocol to measure, and (b) radial pressure exerted by scaffold specimens at designated T_m. "Black *" $p < 0.05$ comparing *linear-* and *star-* scaffolds of same M_n. "Blue *" $p < 0.05$ versus 10kℓ. "Pink *" $p < 0.05$ versus 10k★.

In bone tissue regeneration, a scaffold should not impede neotissue formation ($\sim$8–12 weeks),[39,40] whereas gynecological stents that are resorbed ($\sim$1–3 months) may eliminate postoperative removal.[14,41] Degradation rates of scaffolds were evaluated under base-catalyzed conditions *via* gravimetric (Fig. 4a–d, and Table S8, ESI†), visual inspection (Fig. 4e and f), and SEM imaging (Fig. S9, ESI†) assessments. As expected, % crystallinity and crosslink density were linked to the observed relative degradation rates. For a given M_n, *star-* scaffolds degraded faster *versus linear-* scaffolds due to the reduction in % crystallinity, despite a higher crosslink density. This was particularly true of 7.5k★ and 5k★. As M_n was decreased from 10 to 7.5 kg mol^{-1}, 7.5kℓ degraded somewhat faster *versus* 10kℓ, likely stemming from the former's lower crystallinity. However, the 5kℓ exhibited the slowest relative degradation rate due its relatively high crosslink density as well as significant % crystallinity. The fastest rate of degradation was observed for 5k★ which, while having the greatest crosslink density, had the lowest % crystallinity.

Mechanical properties

The mechanical properties of SMP scaffolds are important to the utility in various shape-actuating device applications. For instance, modulus reflects the stiffness or resistance to deformation. Thus, static compressive testing was performed to determine compressive modulus (E), compressive strength (CS), and toughness (Fig. 5). Non-brittleness was confirmed for all scaffolds due to a lack of fracture at maximum strain ($\varepsilon = 85\%$). As with the aforementioned properties, % crystallinity and crosslink density
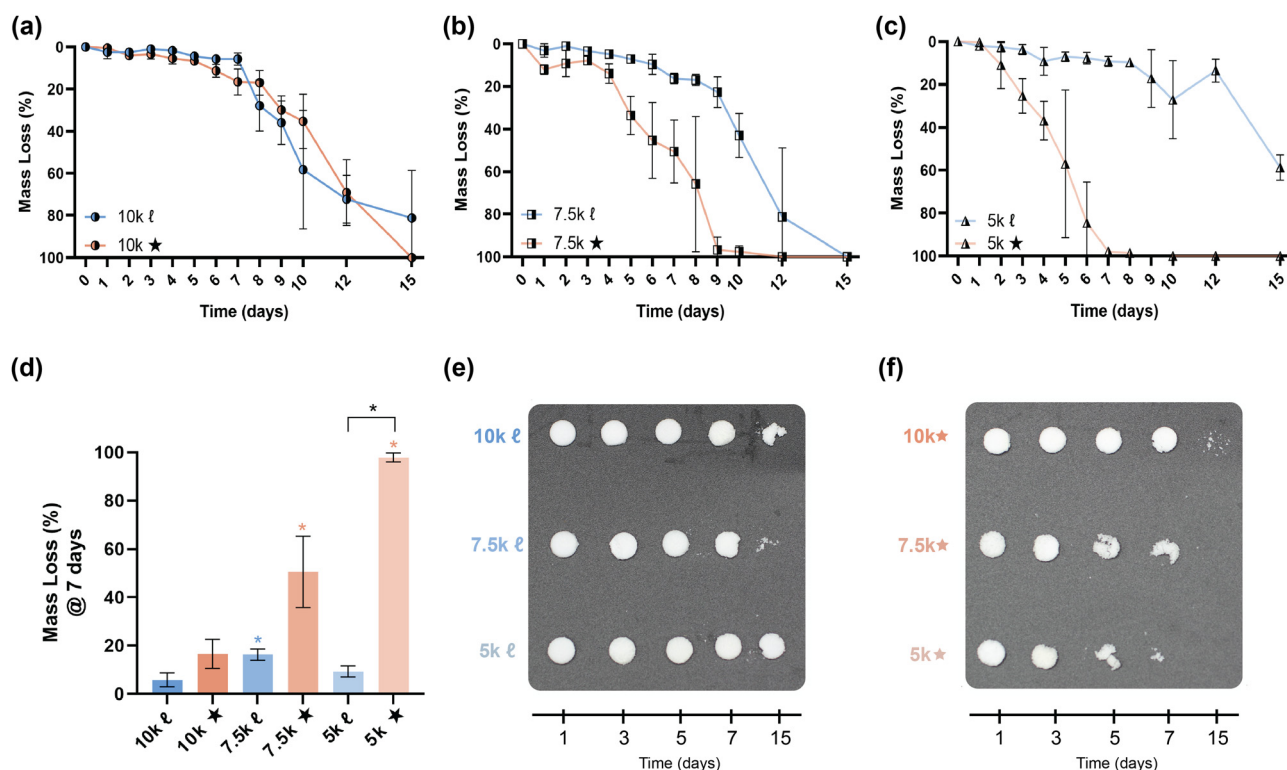

Fig. 4 Base-catalyzed (0.1 M NaOH, 37 °C) degradation studies of scaffolds prepared from (a) 10 kg mol^{-1}, (b) 7.5 kg mol^{-1}, and (c) 5 kg mol^{-1} macromers. (d) Mass loss at 7 days. (e) and (f) Representative photos of specimens at different timepoints. "Black *" $p < 0.05$ comparing *linear-* and *star-* scaffolds of same M_n. "Blue *" $p < 0.05$ versus 10kℓ. "Pink *" $p < 0.05$ versus 10k★.

3700 | *J. Mater. Chem. B*, 2024, **12**, 3694–3702

This journal is © The Royal Society of Chemistry 2024

Fig. 5 Compressive (a) modulus, (b) strength (at $\varepsilon = 85\%$), and (c) toughness of scaffolds. "Black *" $p < 0.05$ comparing *linear*- and *star*- scaffolds of same M_n. "Blue *" $p < 0.05$ *versus* 10kℓ. "Pink *" $p < 0.05$ *versus* 10k★.

produced differences among scaffolds. *Linear*- scaffolds provided the highest (and statistically similar) E values (~ 4.7–7 MPa), attributed to their highest % crystallinity (~ 35–47%). For a given M_n, *star*- scaffolds exhibited significantly lower E values *versus* *linear*- scaffolds: 10k★ (~ 2.0 MPa; 26%), 7.5k★ (1.3 MPa; 22%), and 5k★ (~ 0.69 MPa; $\sim 18\%$). For the *star*- scaffolds, this general decrease in E with decreasing M_n is also attributed to a reduction in % crystallinity, despite the higher crosslink density. Similar trends were also observed for other mechanical properties. The CS and toughness of *linear*- scaffolds (~ 28–33 MPa; ~ 4.3–5.2 MJ m^{-3}) was substantially greater than that of *star*- scaffolds (~ 5.4–10.6 MPa; ~ 0.86–1.8 MJ m^{-3}). While *star*- scaffolds were not as robust, their properties still exceed that of hydrogels that are often explored for implanted medical devices (*e.g.*, poly(ethylene

glycol)-DA [3.4 kg mol^{-1}]: $E \sim 0.2$ MPa, CS = ~ 0.13 MPa, and toughness = ~ 0.015 MJ m^{-3}).[42]

Conclusions

Shape memory implanted devices, readily created from acrylated PCL macromers, hold potential for broad utility stemming from the ability to undergo thermally-triggered shape actuation. For instance, leveraging shape recovery to undergo expansion within spaces, porous PCL SMP scaffolds could be used as self-fitting bone scaffolds or as self-expanding vaginal stents. Utility in such applications necessitates that thermal triggering be accomplished at temperatures safe to biological tissues or at body temperature. The T_m of PCL serves as its shape actuation temperature. Thus, a self-fitting scaffold would ideally exhibit 37 °C $< T_m <$ 55 °C to allow surgical-site irrigation to prolong the fitting time before returning to a rigid state. A self-expanding vaginal stent should exhibit a $T_m < 37$ °C to enable insertion in a fixed, compressed state followed by *in situ* expansion. In this study, the targeted systematic decreases in PCL scaffold T_m was achieved *via* macromers with a *star* architecture and reductions in M_n. Lower T_m values were expected upon adequately reducing % crystallinity. This was demonstrated with a series of six scaffolds prepared from the designated *linear*-PCL-DA or *star*-PCL-TA macromers of varying M_n: 10kℓ ($M_n \sim 10$ kg mol^{-1}), 7.5kℓ ($M_n \sim 7.5$ kg mol^{-1}), 5kℓ ($M_n \sim 5$ kg mol^{-1}), 10k★ ($M_n \sim 10$ kg mol^{-1}), 7.5k★ ($M_n \sim 7.5$ kg mol^{-1}), and 5k★ ($M_n \sim 5$ kg mol^{-1}). As macromer M_n was reduced, *linear*-scaffolds PCL-DA did not show a reduction in T_m (~ 51–56 °C) owing to insufficient decreases in % crystallinity: 10kℓ ($\sim 46\%$) *versus* 7.5kℓ ($\sim 37\%$) and 5kℓ ($\sim 35\%$). However, *star*-scaffolds exhibited substantial and progressive decreases in T_m as M_n was decreased, imparted by diminished % crystallinity: 10k★ (~ 46 °C/$\sim 27\%$), 7.5k★ (~ 40 °C/$\sim 22\%$), and 5k★ (~ 29 °C/$\sim 19\%$). While crosslink density increased with decreasing M_n, the corresponding reduction of % crystallinity was the driving factor in the observed trends in material properties. *Star*- scaffolds exhibited faster rates of degradation that also increased with decreasing M_n, a feature beneficial to the noted device applications. Due to the reduction of crystallinity, the mechanical properties of *star*- scaffolds were diminished relative to *linear*- scaffolds, but exceeded that of common biomedical hydrogels explored in such applications. The shape memory behavior of *star*- scaffolds were largely retained, with a slight decrease for 5k★. The radial expansion forces of *star*- scaffolds exceeded that of *linear*- scaffolds wherein shape recovery was facilitated by faster melting of the formers' crystalline lamellae present at lower percentages. While the utility of *star*-PCL macromers to impart the desired T_m was demonstrated with porous scaffolds *via* SCPL, this platform may be used in a variety of fabrication methods and final product forms to achieve thermally-modulated shape memory devices with tissue safety.

Author contributions

The manuscript was written through contributions of all authors. All authors have given approval to the final version of the manuscript.

This journal is © The Royal Society of Chemistry 2024

J. Mater. Chem. B, 2024, **12**, 3694–3702 | **3701**

Conflicts of interest

There are no conflicts to declare.

Acknowledgements

References

1 M. R. Pfau and M. A. Grunlan, *J. Mater. Chem. B*, 2021, **9**, 4287–4297.

2 J. Delaey, P. Dubruel and S. Van Vlierberghe, *Adv. Funct. Mater.*, 2020, **30**, 1909047.

3 R. Dwivedi, S. Kumar, R. Pandey, A. Mahajan, D. Nandana, D. S. Katti and D. Mehrotra, *J. Oral Biol. Craniofac. Res.*, 2020, **10**, 381–388.

4 M. Labet and W. Thielemans, *Chem. Soc. Rev.*, 2009, **38**, 3484–3504.

5 M. C. Serrano and G. A. Ameer, *Macromol. Biosci.*, 2012, **12**, 1156–1171.

6 J. Delaey, P. Dubruel and S. Van Vlierberghe, *Adv. Funct. Mater.*, 2020, **30**, 1909047.

7 D. Zhang, O. J. George, K. M. Petersen, A. C. Jimenez-Vergara, M. S. Hahn and M. A. Grunlan, *Acta Biomater.*, 2014, **10**, 4597–4605.

8 L. N. Nail, D. Zhang, J. L. Reinhard and M. A. Grunlan, *J. Visualized Exp.*, 2015, **105**, e52981.

9 M. R. Pfau, F. O. Beltran, L. N. Woodard, L. K. Dobson, S. B. Gasson, A. B. Robbins, Z. T. Lawson, W. B. Saunders, M. R. Moreno and M. A. Grunlan, *Acta Biomater.*, 2021, **136**, 233–242.

10 M. Can, S. Koluaçik, E. Bahçe, H. Gokce and F. S. Tecellioglu, *J. Mech. Behav. Biomed. Mater.*, 2022, **126**, 105030.

11 G. Augustin, T. Zigman, S. Davila, T. Udilljak, T. Staroveski, D. Brezak and S. Babic, *Clin. Biomech.*, 2012, **27**, 313–325.

12 K. Kurata, J. Matsushita, A. Furuno, J. Fujino and H. Takamatsu, *J. Orthop. Res.*, 2017, **35**, 2799–2807.

13 E. B. Dolan, M. G. Haugh, M. C. Voisin, D. Tallon and L. M. McNamara, *PLoS One*, 2015, **10**, e0119652.

14 M. Wancura, J. M. McCracken, E. Steen, E. Cosgriff-Hernandez, S. Keswani and J. C.-E. Hakim, *Curr. Opin. Gynecol. Obstet.*, 2019, **31**, 309–316.

15 A. Kamatar, A. Robinson, C. Roberts, F. Beltran, J. McCracken, M. Grunlan, J. Hakim and E. Cosgriff-Hernandez, *Society for Biomaterials*, Baltimore, MD, 26–30, 2022.

16 L. Peponi, I. Navarro-Baena, J. E. Báez, J. M. Kenny and A. Marcos-Fernandez, *Polymer*, 2012, **53**, 4561–4568.

17 I. Navarro-Baena, A. Marcos-Fernández, A. Fernández-Torres, J. M. Kenny and L. Peponi, *RSC Adv.*, 2014, **4**, 8510–8524.

18 Y. Ren, Z. Wei, X. Leng, T. Wu, Y. Bian and Y. Li, *J. Phys. Chem. B*, 2016, **120**, 4078–4090.

19 S. Corneillie and M. Smet, *Polym. Chem.*, 2015, **6**, 850–867.

20 J. M. Ren, T. G. McKenzie, Q. Fu, E. H. H. Wong, J. T. Xu, Z. S. An, S. Shanmugam, T. P. Davis, C. Boyer and G. G. Qiao, *Chem. Rev.*, 2016, **116**, 6743–6836.

21 R. J. Mondschein, A. Kanitkar, C. B. Williams, S. S. Verbridge and T. E. Long, *Biomaterials*, 2017, **140**, 170–188.

22 Y. Sakamoto and H. Tsuji, *Polymer*, 2013, **54**, 2422–2434.

23 E. S. Kim, B. C. Kim and S. H. Kim, *J. Polym. Sci. Polym. Phys.*, 2004, **42**, 939–946.

24 X. Y. Zhu, Y. F. Zhou and D. Y. Yan, *J. Polym. Sci. Polym. Phys.*, 2011, **49**, 1277–1286.

25 M. R. Pfau, K. G. McKinzey, A. A. Roth, L. M. Graul, D. J. Maitland and M. A. Grunlan, *J. Mater. Chem. B*, 2021, **9**, 3826–3837.

26 Y. Li and T. Kissel, *Polymer*, 1998, **39**, 4221–4447.

27 A. Breitenbach, Y. X. Li and T. Kissel, *J. Controlled Release*, 2000, **64**, 167–178.

28 J. Burke, R. Donno, R. d'Arcy, S. Cartmell and N. Tirelli, *Biomacromolecules*, 2017, **18**, 728–739.

29 J. F. Douglas, J. Roovers and K. F. Freed, *Macromolecules*, 1990, **23**, 4168–4180.

30 Y. Lu, L. J. An and Z. Wang, *Macromolecules*, 2013, **46**, 5731–5740.

31 M. T. Frassica, S. K. Jones, P. Diaz-Rodriguez, M. S. Hahn and M. A. Grunlan, *Acta Biomater.*, 2019, **99**, 100–109.

32 C. G. Pitt, F. I. Chasalow, Y. M. Hibionada, D. M. Klimas and A. Schindler, *J. Appl. Polym. Sci.*, 1981, **26**, 3779–3787.

33 M. A. Wierzbicki, J. Bryant, M. W. Miller, B. Keller and D. J. Maitland, *J. Mech. Behav. Biomed. Mater.*, 2016, **59**, 156–167.

34 N. Abbasi, S. Hamlet, R. M. Love and N. T. Nguyen, *J. Sci. Adv. Mater. Dev.*, 2020, **5**, 1–9.

35 Y. Shirakata, T. Nakamura, Y. Shinohara, K. Taniyama, K. Sakoda, T. Yoshimoto and K. Noguchi, *J. Mater. Sci.: Mater. Med.*, 2014, **25**, 899–908.

36 C. Bosch, B. Melsen and K. Vargervik, *J. Craniofac. Surg.*, 1998, **9**, 310–316.

37 A. Bandyopadhyay, P. K. Valavala, T. C. Clancy, K. E. Wise and G. M. Odegard, *Polymer*, 2011, **52**, 2445–2452.

38 B. D. Ulery, L. S. Nair and C. T. Laurencin, *J. Polym. Sci. Polym. Phys.*, 2011, **49**, 832–864.

39 E. Gomez-Barrena, P. Rosset, D. Lozano, J. Stanovici, C. Ermthaller and F. Gerbhard, *Bone*, 2015, **70**, 93–101.

40 M. S. Ghiasi, J. Chen, A. Vaziri, E. K. Rodriguez and A. Nazarian, *Bone Rep.*, 2017, **6**, 87–100.

41 G. M. Grimsby and L. A. Baker, *Curr. Urol. Rep.*, 2014, **15**, 428.

42 M. T. Frassica, C. J. Demott, E. M. Ramirez and M. A. Grunlan, *ACS Macro Lett.*, 2020, **9**, 1740–1744.

3702 | *J. Mater. Chem. B*, 2024, **12**, 3694–3702

This journal is © The Royal Society of Chemistry 2024